Supplementary Information for:

Spatially controlled octahedral rotations and metal-insulator transitions in nickelate superlattices

Binbin Chen[1], Nicolas Gauquelin[2], Robert J. Green[3,4], Jin Hong Lee[5], Cinthia Piamonteze[6], Matjaž Spreitzer[7], Daen Jannis[2], Johan Verbeeck[2], Manuel Bibes[5], Mark Huijben[1], Guus Rijnders[1], Gertjan Koster[1]*

[1]MESA+ Institute for Nanotechnology, University of Twente, 7500 AE Enschede, The Netherlands

[2]Electron Microscopy for Materials Science (EMAT), University of Antwerp, 2020 Antwerp, Belgium

[3]Department of Physics and Engineering Physics, University of Saskatchewan, 116 Science Pl, Saskatoon, Saskatchewan S7N 5E2, Canada

[4]Stewart Blusson Quantum Matter Institute, University of British Columbia, 111-2355 E Mall, Vancouver, British Columbia V6T 1Z4, Canada

[5]Unité Mixte de Physique, CNRS, Thales, Univ. Paris-Sud, Université Paris-Saclay, 91767 Palaiseau, France

[6]Swiss Light Source, Paul Scherrer Institute, 5232 Villigen PSI, Switzerland

[7]Advanced Materials Department, Jožef Stefan Institute, 1000 Ljubljana, Slovenia

*To whom correspondence should be addressed

E-mail: g.koster@utwente.nl

MATERIALS AND METHODS

Sample growth and characterization. The pulsed laser depositions were conducted using a relatively high laser fluence of 2 J/cm^2 to insure the right stoichiometry of $NdNiO_3$.[1] The oxygen pressure and repetition rate were fixed at 0.2 mbar and 2 Hz, respectively. The substrate temperature was kept at 700 ºC. After the deposition, the samples were in-situ annealed for 15 min to improve the crystallinity before cooling down to room temperature. The single terminated $NdGaO_3$ substrates were obtained by chemical etching with buffered HF, followed by annealing at 1050 ºC for 2 hours in oxygen flow.[2] The X-ray diffractions were performed on PANalytical-X'Pert materials research diffractometer at the high-resolution mode. The surface morphology was characterized by atomic force microscopy. Transport properties were measured using a van der Pauw geometry on the Quantum Design physical property measurement system. The resistivities of the superlattices are calculated using the actual thickness of $NdNiO_3$ since the growth at high oxygen pressure produces insulating $SrTiO_3$ layers.

Scanning transmission electron microscopy. The characterization of the atomic structure was conducted using Cs-corrected scanning transmission electron microscopy high angle dark field imaging (STEM-HAADF) on the X-Ant-Em instrument at the University of Antwerp operated at 300kV, a convergence angle of 20 mrad and a collection angle of 44-190 mrad. The samples were cut along the orthorhombic [001] direction of $NdGaO_3$ substrates using a FEI Helios 650 dual-beam Focused Ion Beam device. Chemical mapping was performed using electron energy loss spectroscopy (EELS) on a Gatan Quantum ERS spectrometer with a collection angle of 85 mrad, an exposure time of 80 ms/pixel and a 0.5 eV/pixel dispersion in dual EELS mode. Raw data is presented after power-law background subtraction. Further details can also be found here[3]

Resonant magnetic diffraction. The resonant magnetic diffraction experiments were performed using an in-vacuum 4-circle diffractometer with chamber pressure below 10^{-9} Torr at the resonant elastic and inelastic X-ray scattering beamline at Canadian light source in Saskatoon, Canada. The beamline has a flux of 5×10^{12} photon s^{-1} and energy resolution of 10^{-4} eV. During the angular scan, the energy of the incident X-ray was set to 853.3 eV, which is at the Ni L_3 maximum.

X-ray absorption spectroscopy. The XAS experiments were performed at the X-Treme beamline of the Swiss Light Source.[4] The data were collected using the total electron yield mode, with incoming X-ray at an angle of 30° from the sample surface. The spectra shown in Figure 4 were obtained by averaging four successive spectra measured with π and σ linear polarizations.

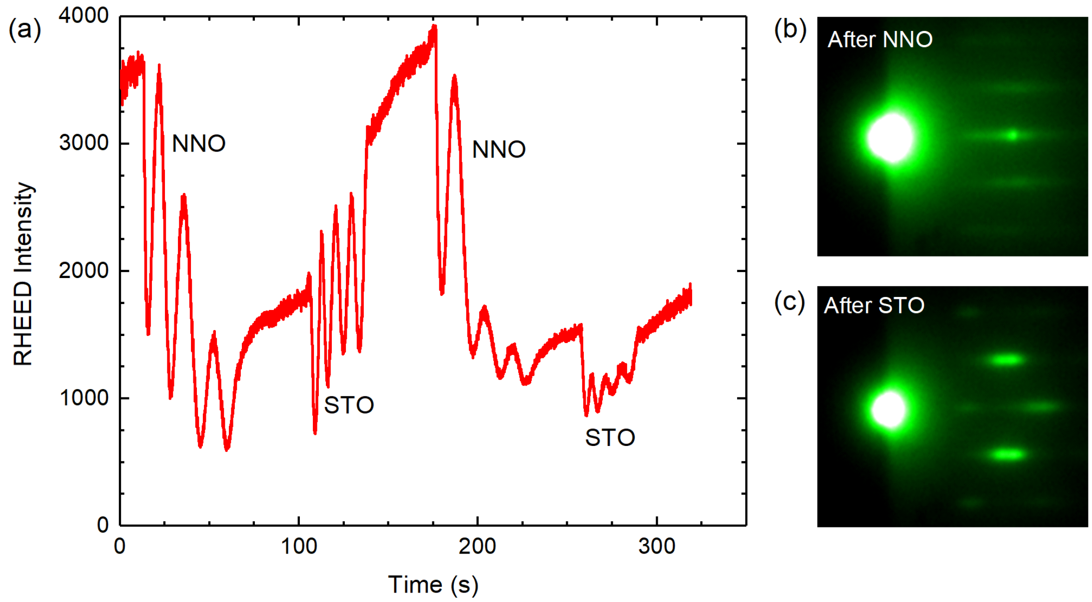

Figure S1. (a) Typical RHEED intensity profile recorded during the growth of NNO/STO SL with n = 4. The RHEED patterns taken after the last NNO and STO layers are shown in (b) and (c), respectively.

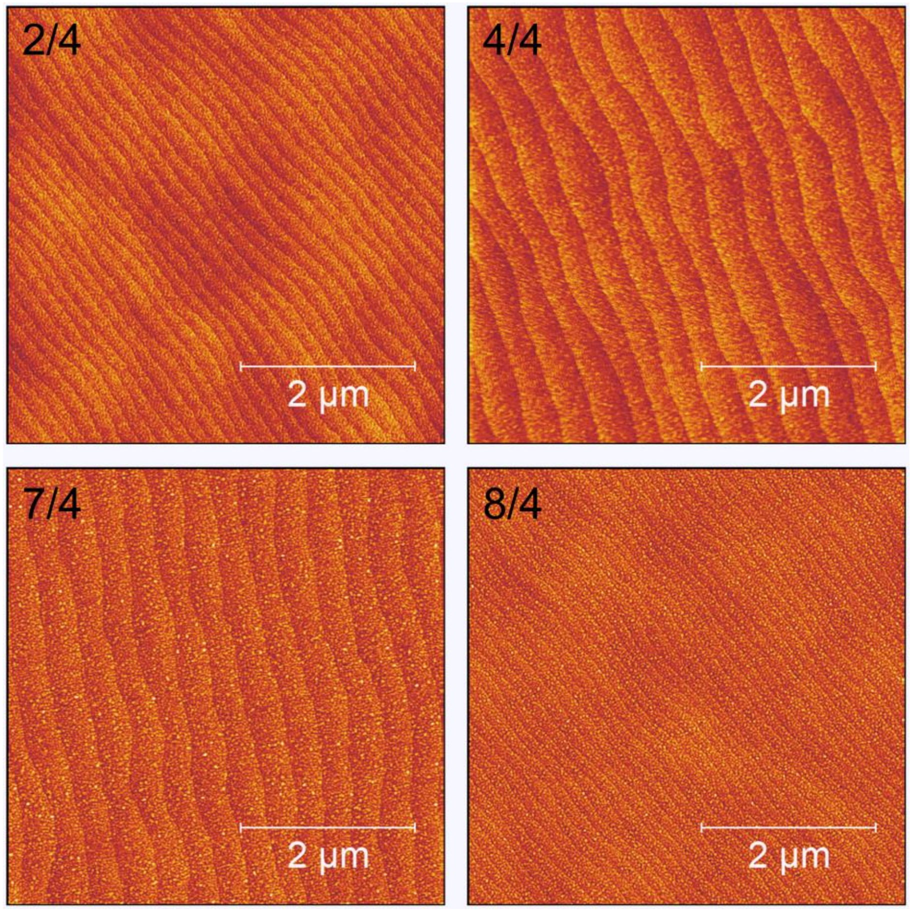

Figure S2. AFM images of the NNO/STO SLs with n = 2, 4, 7 and 8. The step-terrace surface confirms the high crystalline ordering of our samples.

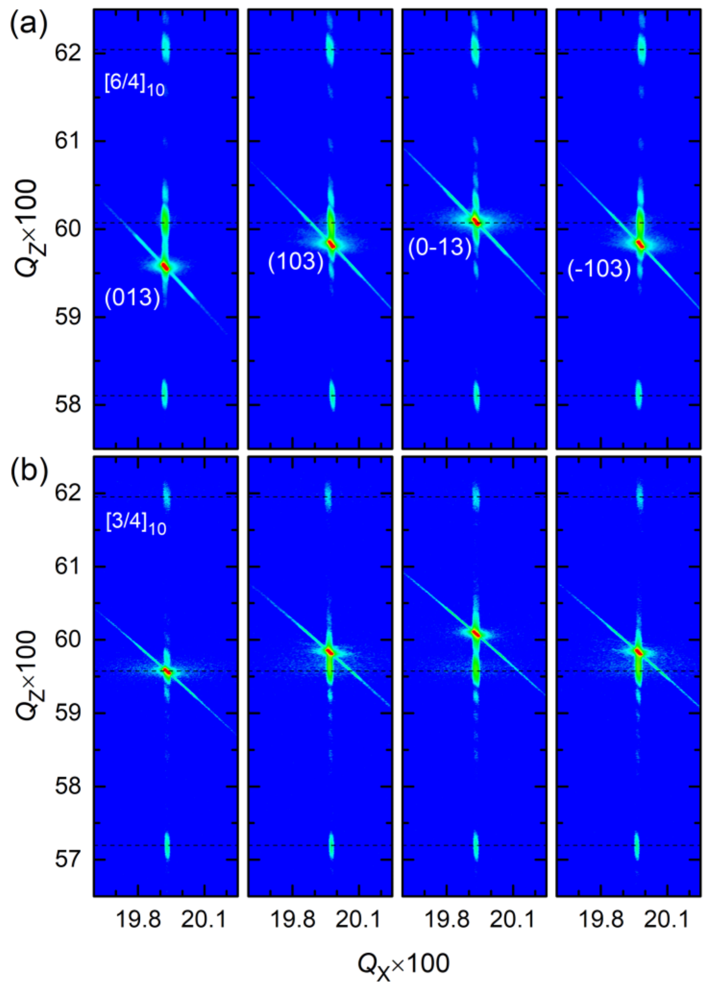

Figure S3. RSMs around pseudocubic (013), (103), (0-13), and (-103) reflections measured from the NNO/STO SLs with n = 6 (a) and n = 3 (b). Both SLs share the same Q_X value with the NGO substrates, indicative of their coherently strained state. The four reflections show the same Q_Z value for both SLs with n = 6 and n = 3, attesting to their tetragonal symmetry.

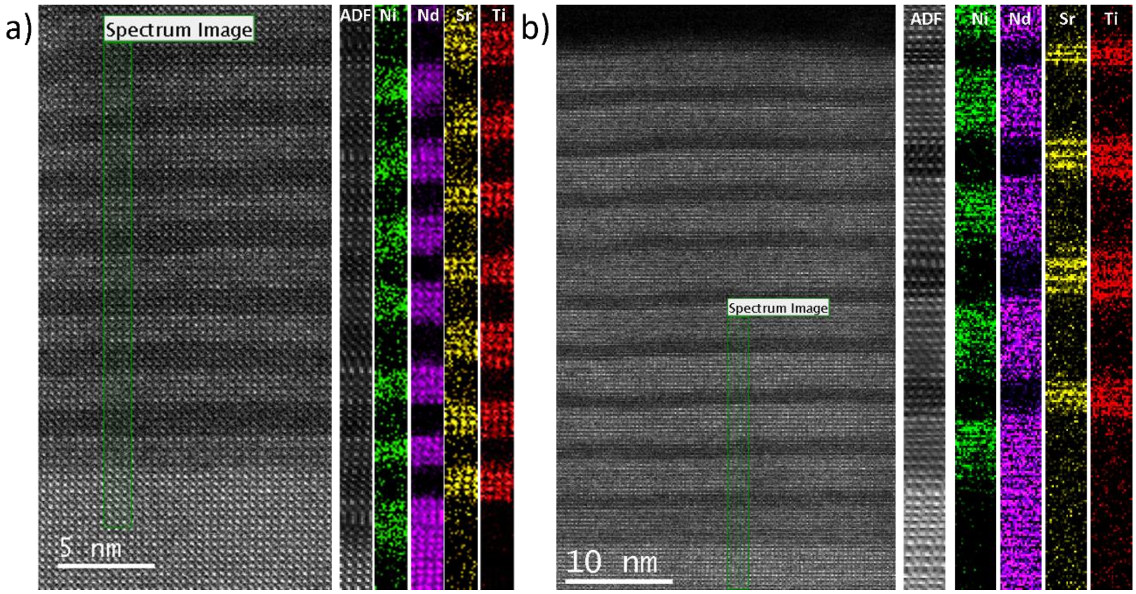

Figure S4. Low-magnification STEM images of NNO/STO SLs with n = 4 (a) and n = 8 (b). The atomically resolved EELS mappings of Ni (green), Nd (purple), Sr (yellow) and Ti (red) are shown on the right side, along with the annular dark filed (ADF) images.

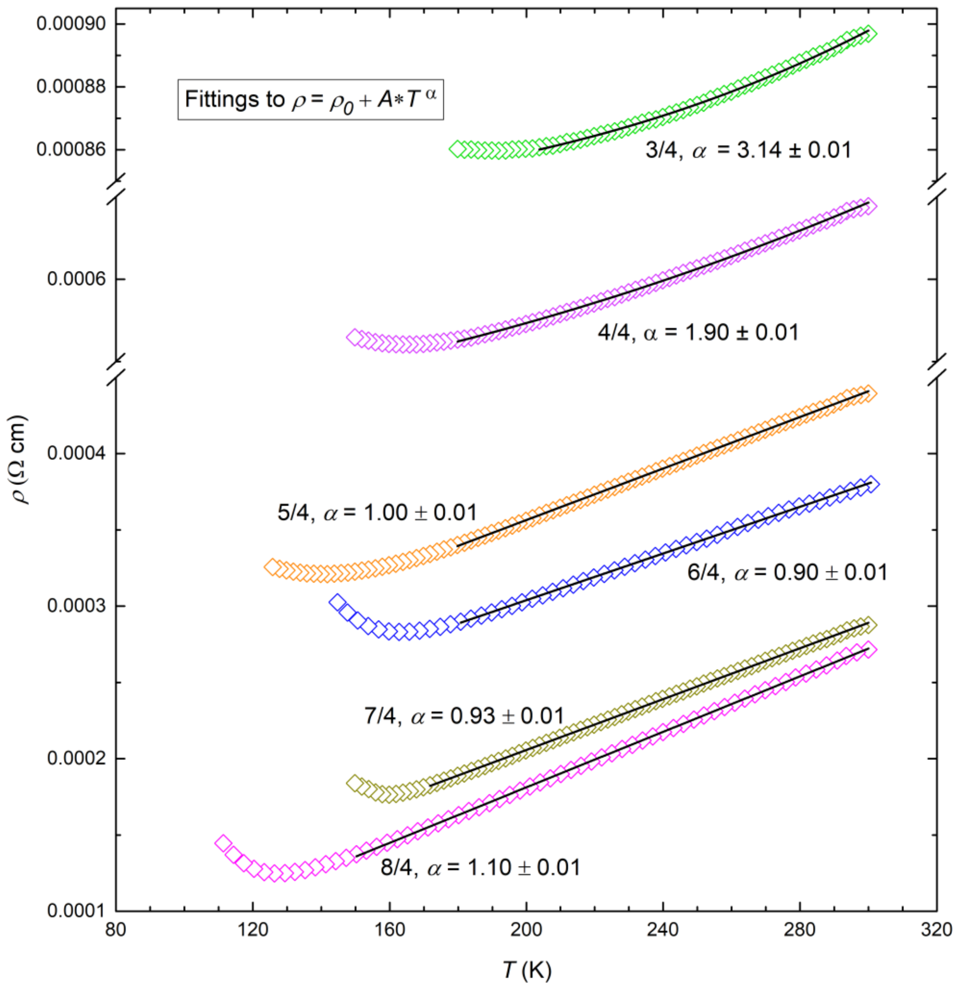

Figure S5. Fittings of the metallic resistivity for the SLs with $n \geq 3$ to a power law $\rho = \rho_0 + A * T^{\alpha}$. The exponent α is determined as described in Ref. 5.

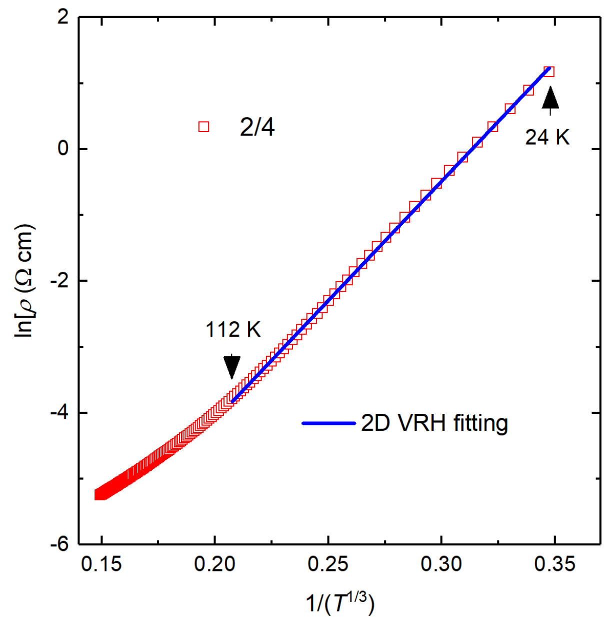

Figure S6. Fitting of the resistivity of the n = 2 SL to the 2D-VRH mechanism, $\rho = \rho_0 \exp[(T_0/T)^{1/3}]$. Here T_0 is derived as 4.75×10^4 K. The mean hopping energy estimated by $E_0 = 1/3k_BT^{2/3}T_0^{1/3}$ is larger than k_BT in the fitting temperature range, validating the use of a 2D-VRH model.[6] Such a conduction mechanism can persist to relatively high temperature because of the possible polaron-assisted electron hopping.[7]

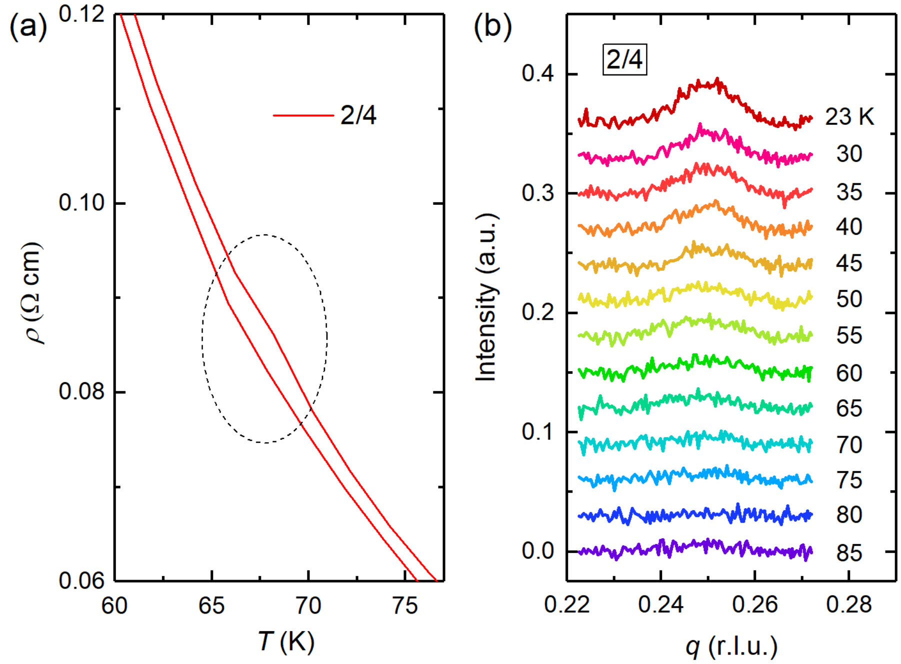

Figure S7. (a) Enlarged view of the temperature dependent resistivity curve for the $n = 2$ SL to highlight the anomaly around ~68 K. (b) Isothermal rocking curves around $q = (¼, ¼, ¼)_{pc}$ reflection of the $n = 2$ SL measured by x-ray resonant magnetic diffraction.

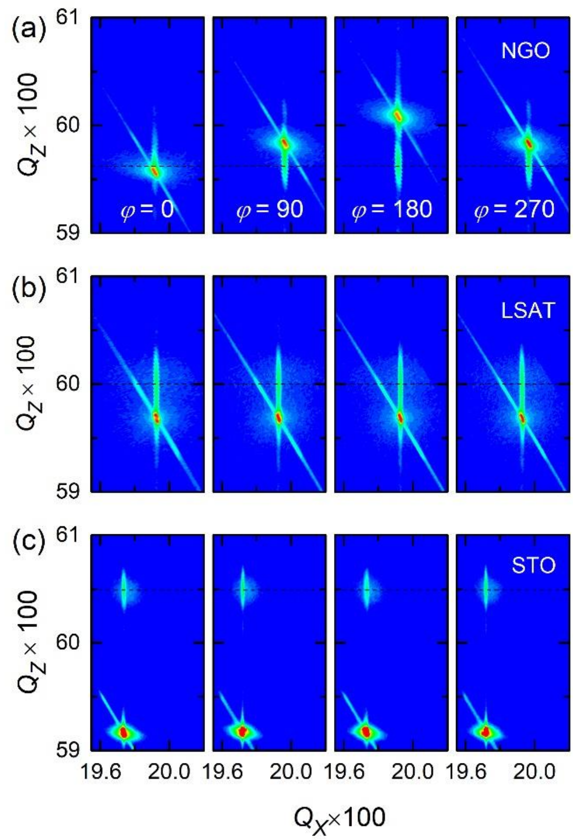

Figure S8. RSMs of the (103) reflection measured at four successive φ angles for the n = 5 SLs grown on NGO $(001)_{pc}$ (a), LSAT (001) (b) and STO (001) (c).

References:

(1) Breckenfeld, E.; Chen, Z.; Damodaran, A. R.; Martin, L. W. Effects of Nonequilibrium Growth, Nonstoichiometry, and Film Orientation on the Metal-to-Insulator Transition in $NdNiO_3$ Thin Films. *ACS Appl. Mater. Interfaces* **2014**, *6* (24), 22436–22444.

(2) Leca, V.; Blank, D. H. A.; Rijnders, G. Termination Control of $NdGaO_3$ Crystal Surfaces by Selective Chemical Etching. arXiv:1202.2256v2 (2012).

(3) J Wang, Y Shin, N Gauquelin, Y Yang, C Lee, D Jannis, J. Verbeeck, J.M. Rondinelli and S.J. May, Physical properties of epitaxial SrMnO2. 5− δ F γ oxyfluoride films, Journal of Physics: Condensed Matter 31 (36), 365602

(4) Piamonteze, C.; Flechsig, U.; Rusponi, S.; Dreiser, J.; Heidler, J.; Schmidt, M.; Wetter, R.; Calvi, M.; Schmidt, T.; Pruchova, H.; Krempasky, J.; Quitmann, C.; Brune, H.; Nolting, F. X-Treme Beamline at SLS: X-ray Magnetic Circular and

Linear Dichroism at High Field and Low Temperature. *J. Synchrotron Radiat.* **2012**, *19*, 661–674.

(5) Guo, Q.; Farokhipoor, S.; Magén, C.; Rivadulla, F.; Noheda, B. Tunable Resistivity Exponents in the Metallic Phase of Epitaxial Nickelates. *Nat. Commun.* **2020**, 11, 2949.

(6) Wei, H.; Jenderka, M.; Bonholzer, M.; Grundmann, M.; Lorenz, M. Modeling the Conductivity around the Dimensionality-Controlled Metal-Insulator Transition in $LaNiO_3/LaAlO_3$ (100) Superlattices. *Appl. Phys. Lett.* **2015**, 106, 042103.

(7) Scherwitzl, R.; Gariglio, S.; Gabay, M.; Zubko, P.; Gibert, M.; Triscone, J.-M. Metal-Insulator Transition in Ultrathin $LaNiO_3$ Films. *Phys. Rev. Lett.* **2011**, *106*, 246403.